RSC Advances

ROYAL SOCIETY OF CHEMISTRY

www.rsc.org/advances

Electrodeposited Nickel Cobalt Sulfide Nanosheet Arrays on 3D-graphene/Ni foam for High-Performance Supercapacitors

Yang Wang,[a] Lidong Wang,[a] Bing Wei,[a] Qinghua Miao,[a] Yinan Yuan,[a] Ziyue Yang,[a] Weidong Fei [a,*]

[a] *School of Materials Science and Engineering, Harbin Institute of Technology, Harbin 150001, China.*

* Corresponding author at: School of Materials Science and Engineering, Harbin Institute of Technology, Harbin 150001, China.

E-mail address: wdfei@hit.edu.cn (W. Fei).

Herein, graphene oxide (GO) with a 3D structure was prepared on the surface of Ni foam (NF) via electrophoretic deposition and then reacted in-situ to form 3D reduced graphene oxide (RGO) via thermal reduction. Ni-Co-S nanosheet arrays were produced on various substrates (RGO/NF, GO/NF and NF) via a facile one-step electrochemical deposition. Scanning electron microscopy (SEM) demonstrated that RGO nanosheets were vertically wrapped on NF by thermal reduction of GO. Furthermore, interconnected and hierarchical porous Ni-Co-S nanosheets were uniformly coated on RGO. The electrochemical performance of the ternary material on different substrates was investigated. The physical structures combined with the advantages of both ternary Ni-Co-S and RGO exhibited excellent electrochemical performance. Incorporated as electrode materials for supercapacitors, the synthesized samples possess high specific capacitance and a long cycle life. With the synergistic effect of RGO and ternary Ni-Co-S, the high performance is achieved. The specific capacitance of Ni-Co-S/RGO/NF (2643 F g^{-1}) demonstrated an enhancement compared with Ni-Co-S/GO/NF (2083 F g^{-1}) and Ni-Co-S/ NF (1329 F g^{-1}) at a current density of 10 A g^{-1}. Additionally, the retention of specific capacitance of Ni-Co-S/RGO/NF after 2500 cycles displayed superior cyclic stability of 84.22 % at a current density of 50 A g^{-1}.

1. Introduction

With the rapid advancement of technology in society as well as the ever-increasing of population, the electrical demand is quickly becoming a dilemma. Thus, it is urgent to develop an environmentally green energy source that is an adequate substitute for fossil fuels. Meanwhile, it is also essential to investigate new energy conversion and storage devices to utilize energy in the most efficient manner possible.[1-3] Because of their advantages of rapid charge-discharge, high power density and long cycle life, supercapacitors have attracted much attention in recent years. Depending on the energy storage mechanism, supercapacitors can be classified as either electric double layer capacitors (EDLCs), pseudocapacitors, or a combination of the two.[4, 5] EDLCs are electrochemical capacitors in which energy storage is primarily achieved by separation of charge via a Helmholtz double layer at the interface between the surface of a conductor electrode and an electrolytic solution electrolyte.[6, 7] Pseudocapacitors store electrical energy via redox reactions on the surface of the electrode by adsorbed ions that results in a reversible faradic charge-transfer on the electrode; generally speaking, pseudocapacitors possess a larger capacitance than EDLCs.[8]

Graphene, an atomic-scale honeycomb lattice composed of carbon atoms, has been extensively studied for the past decade due to its high electrical conductivity, high theoretical specific surface area, chemical stability and cost effectiveness.[9, 10] Graphene demonstrates moderate capacitance due to its electric double layer storage mechanism. Many transition metal oxides (MnO_2, NiO, Co_3O_4, ect.) are suitable materials for pseudocapacitors with a higher capacitance.[11-16] However, transition metal oxides have poor electrical conductivity, which limits the cycle stability of the supercapacitor.[8] More recently, ternary Ni-Co-S materials have been intensively studied owing to their advantageous characteristics of high capacitance, enhanced redox reaction, low toxicity and low cost relative to NiS, CoS, Co_9S_8.[17, 18] Results also demonstrated an optimized ternary material of $NiCo_2S_4$ that exhibited a higher electrical conductivity than $NiCo_2O_4$.[19-21] Consequently, ternary Ni-Co-S materials have great potential in the development of supercapacitors. Ternary Ni-Co-S materials are typically synthesized via a 2-step hydrothermal reaction.[18, 22, 23] As a comparable method, electrochemical deposition is used to synthesize ternary Ni-Co-S materials on carbon cloth and 2D-graphene/NF.[24, 25]

Chen and coworkers[24] reported that the capacitance of Ni-Co-S/carbon cloth is 1418 F g^{-1} at 5 A g^{-1}. Nguyen and coworkers[25] reported that 2D-graphene, produced via CVD method, could be coated on Ni foam (NF) to produce a graphene/NF substrate in which ternary Ni-Co-S material can be deposited via electrochemical deposition. The microstructures of both carbon cloth and graphene/NF are 2-dimentional possessing a low surface area. Compared with a 2-dimentional architecture, 3D microstructure graphene substrates have the potential to provide a higher surface for the deposition of Ni-Co-S and shorter ion channel lengths for electrolyte, which

benefits the performance of the electrode. Thus, it is reasonable to expect that Ni-Co-S/3D graphene electrode could demonstrate superior electrochemical performance.[15]

Herein, 3D GO nanosheets were vertically coated onto the surface of NF via electrophoretic deposition and then 3D GO was reacted to form 3D RGO via in-situ thermal reduction. Subsequently, we loaded the ultrathin, flowerlike, interconnected and hierarchical porous ternary Ni-Co-S nanosheets onto RGO/NF via a facile route of one-step electrochemical deposition. With the synergistic effect of 3D RGO and Ni-Co-S nanosheets, the Ni-Co-S/RGO/NF electrode exhibits excellent electrochemical performance.

2. Experimental section

2.1. Materials

All the reagents used in the experiment were of analytical grade. Natural graphite powder (99 %, 45 μm) was purchased from Qingdao Jinrilai Graphite Co., Ltd.. The potassium permanganate ($KMnO_4$), hydrogen peroxide (H_2O_2, 30 %), cobalt chloride hexahydrate ($CoCl_2·6H_2O$), nickel chloride hexahydrate ($NiCl_2·6H_2O$) and thiourea ($CS(NH_2)_2$) were purchased from Sinopharm Chemical Reagent Co., Ltd. Sulfuric acid (H_2SO_4, 98 %) and phosphoric acid (H_3PO_4, 85 %) were purchased from Beijing Chem. Co., Ltd.. All materials were used as obtained without further purification. NF (99.6 %，1.7 mm in thickness) was purchased from Kunshan Bitaixiang Electronics Co., Ltd. and cut into small pieces with a dimension of 10×10×1.7 mm.

2.2 Production of RGO/NF

NF was cleaned with acetone by ultrasonication for 30 min and rinsed with deionized water and ethanol for several times and then dried at 60 ℃ for 1 h. GO was prepared by the modified Hummer's method.[26, 27] Subsequently, GO/NF was produced via electrophoretic deposition. NF was used as the positive electrode and Ti foil as the negative electrode; the electrophoretic voltage was 3 V and the concentration of GO solution was 1 mg ml^{-1}. The GO/NF was rinsed with deionized water several times and then dried at 60 ℃ for 2 h by a vacuum oven. Finally, the GO/NF was thermally annealed at 400℃ for 2 h at a heating rate of 10 ℃ in a tube furnace and cooled to room temperature under a gas flow of H_2/Ar (ratio 1:1, flow rate of 50 sccm), during which GO was reduced to RGO to prepare RGO/NF. The preparation process of RGO/NF is illustrated in Fig.1 (a) and (b).

2.3. Synthesis of Ni-Co-S nanosheets

The Ni-Co-S nanosheets were electrochemically deposited onto NF, GO/NF and RGO/NF, separately. The electrolyte solution was prepared by adding 0.36 g of $CoCl_2·6H_2O$, 0.53 g of $NiCl_2·6H_2O$ and 76.35 g of thiourea ($CS(NH_2)_2$) into 300 ml deionized water and ultrasonicated for 15 min. Then, the pH value of solution was adjusted to about 7 with 0.5 M $NH_3·H_2O$ solution.

The electrochemical deposition was carried out in a three-electrode cell using NF, GO/NF or RGO/NF as the working electrode, Pt as the counter electrode, and Ag/AgCl as the reference electrode. Ni-Co-S nanosheets were produced by cyclic voltammetry at a scan rate of 5 mV s^{-1} for 30 cycles within a voltage range of -1.2 V to 0.2 V vs Ag/AgCl reference electrode. Then, the device was rinsed with deionized water several times and dried at 80 ℃ for 12 h in a vacuum oven. Approximately, the masses of Ni-Co-S nanosheet arrays loaded on NF, NF/GO and NF/RGO were 2.3, 2.1 and 1.9 mg cm^{-2}, respectively. The synthetic process of Ni-Co-S/RGO/NF is illustrated in Fig.1 (b) and (c).

The optical photographs of the electrode materials (NF, RGO/NF and Ni-Co-S/RGO/NF) are displayed in Fig. 1. Compared with NF (as shown in Fig. 1(a)), the color of RGO/NF (as shown in Fig. 1(b)) is darker, suggestive of RGO being successfully deposited on the NF. The color of Ni-Co-S/RGO/NF composite in Fig. 1(c) becomes black, indicating successful deposition of the Ni-Co-S material on RGO/NF.

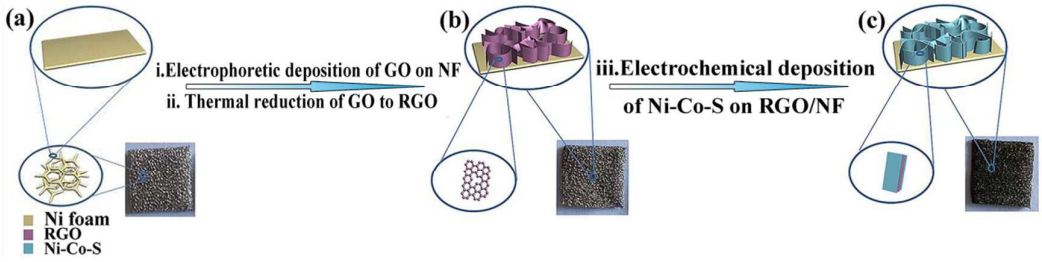

Fig. 1. Schematic illustration of the synthesis process: (a) NF; (b) RGO/NF and (c) Ni-Co-S/RGO/NF, the optical photographs of NF, RGO/NF and Ni-Co-S/RGO/NF are also correspondingly shown.

2.4. Material characterization

The microstructures of NF, GO/NF, RGO/NF and Ni-Co-S/RGO/NF were analyzed by scanning electron microscopy

(SEM, Helios Nanolab 600i) and transmission electron microscopy (TEM, JEM-2100). The energy-dispersive X-ray spectroscopy (EDX) and high-resolution transmission electron microscopy (HRTEM) were performed using JEM-2100. The X-ray photoelectron spectroscopy (XPS) was conducted with a K-alpha (Thermo Fisher) system.

2.5. Electrochemical measurements

Cyclic voltammetry (CV) and galvanostatic charge-discharge (GCD) of Ni-Co-S/NF, Ni-Co-S/GO/NF or Ni-Co-S/RGO/NF were investigated by a CHI760D electrochemical workstation. Electrochemical impedance spectroscopy (EIS) was performed by applying an AC voltage of 5 mV amplitude in the frequency range of 0.1 Hz to 100 kHz with an AutoLab PGSTAT 302N electrochemical analyzer in a three-electrode configuration, in which Ni-Co-S/NF, Ni-Co-S/GO/NF or Ni-Co-S/RGO/NF was implemented as the working electrode; Pt foil and Ag/AgCl were used as the counter electrode and reference electrode, respectively. The electrolyte is 1 M KOH for all the electrochemical tests.

3. Results and discussion

Fig. 2 illustrates the microstructures of pure NF, GO/NF and RGO/NF composites. Compared with pure NF (Fig. 2(a)), in the samples of GO/NF (Fig. 2(c)) and RGO/NF (Fig. 2(e)), the NF substrates were completely covered by GO and RGO. A few small holes can be found on the surface of GO/NF and disappear on the surface of RGO/NF, suggesting a densification process occurred during the process of thermal reduction of GO. The insets of Fig. 2(c) and Fig. 2(e) demonstrate the enlarged microstructures of GO/NF and RGO/NF, which display vertical GO and RGO nanosheet arrays possessing a 3D microstructure wrapped around NF. The 3D structures of GO and RGO can provide substantial contact surface area between the deposited Ni-Co-S material and electrolyte. In addition, the 3D RGO is beneficial for both ion diffusion in the electrolyte and increasing the redox reaction surface area; thus, enabling an achievable high performance of the device. There are abundant flower-like Ni-Co-S nanosheets on the surface of NF, GO/NF and RGO/NF as shown in Fig. 2(b), (d) and (f), respectively. Compared with the Ni-Co-S/RGO/NF and Ni-Co-S/GO/NF, the flower-like clusters on NF are scarcer. The interconnected porous Ni-Co-S nanosheets were vertically wrapped around the GO/NF, RGO/NF and NF substrates. Such flower-like clusters are capable of providing a high contact area with the given electrolyte and decrease the diffusion path for ion transfer. Obviously, compared with the compact structure of Ni-Co-S in Fig. 2(b), the structures of Ni-Co-S in Ni-Co-S/RGO/NF (inset in Fig. 2f) and Ni-Co-S/GO/NF (inset in Fig. 2d) are expanded and may contribute to the enhanced ion diffusion. In addition, compared with the Ni-Co-S in Ni-Co-S/GO/NF electrode, the structure of Ni-Co-S cluster in Ni-Co-S/RGO/NF electrode is smaller and provides a larger redox area. As a result, the Ni-Co-S/RGO/NF electrode possesses the highest performance as discussed in detail in a proceeding section. Due to the thermal and mechanical stress from the electrochemical deposition process, the evidence of cracks were produced on the surface of the electrodes with Ni-Co-S arrays. The elemental mappings of Ni, Co, S and C elements are shown in Fig. 3. It is clear that Ni, Co, S and C elements are uniformly distributed on the sample.

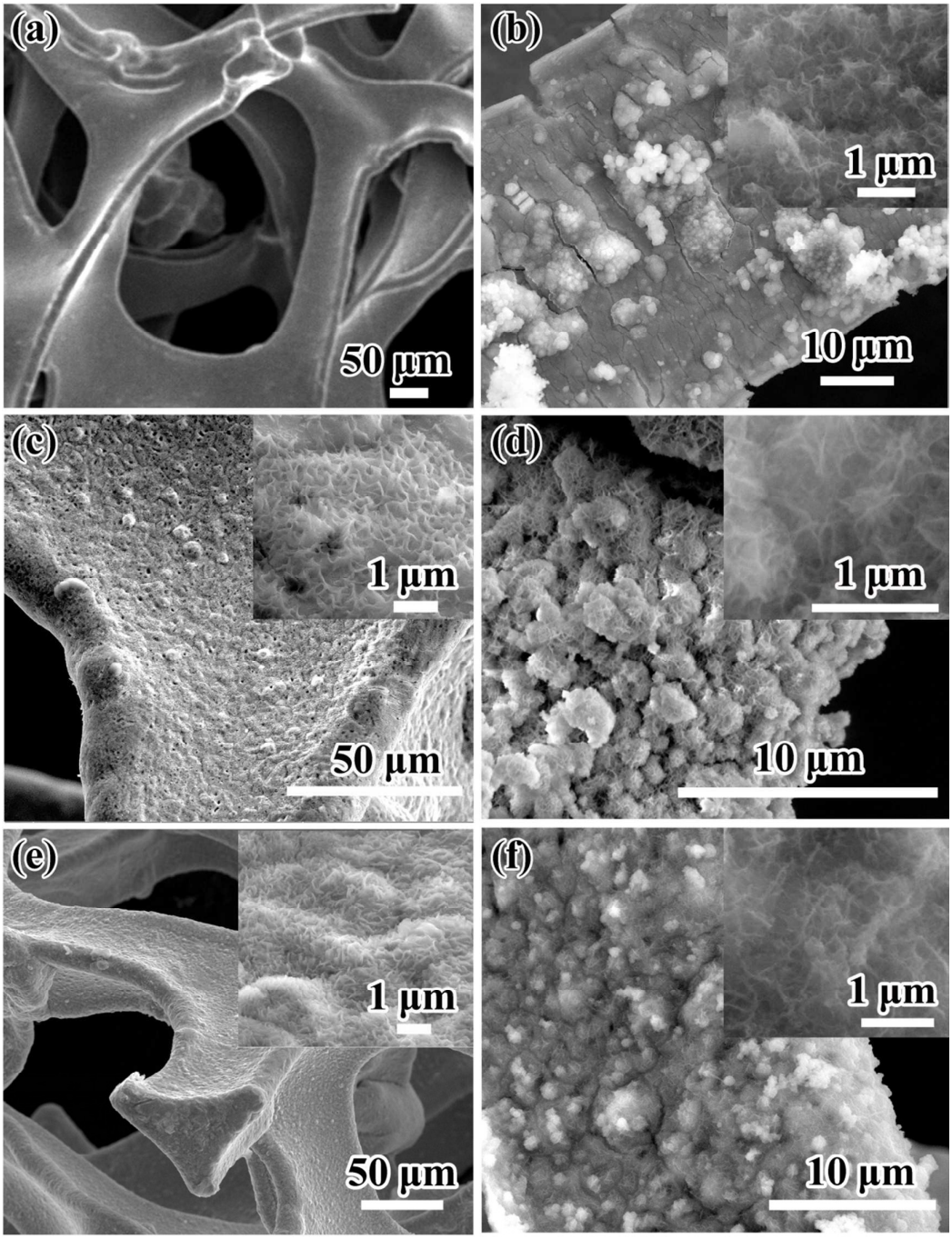

Fig. 2. SEM images: (a) pure NF, (b) Ni-Co-S/NF, (c) GO/NF, (d) Ni-Co-S/GO/NF, (e) RGO/NF, and (f) Ni-Co-S/RGO/NF. Insets depict the corresponding magnification range.

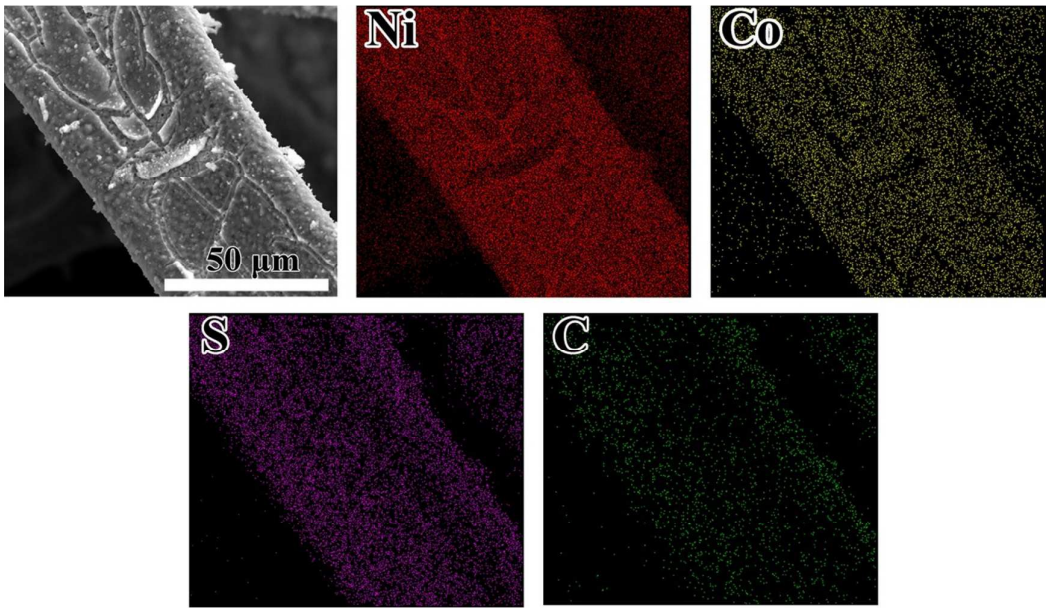

Fig. 3. SEM image and the corresponding Ni, Co, S and C elemental mappings of Ni-Co-S/RGO/NF composite.

The TEM samples were obtained by ultrasound scratching from Ni-Co-S/RGO/NF composite. Fig. 4(a) and (b) display numerous flowerlike clusters with a diameter of about 500 nm are connected with each other; these clusters are composed of many ultrathin nanosheets. A hierarchical porous structure can be seen in Fig. 4(a) that correlates with the SEM image observed in Fig. 2(f). This structure provides large contact surface area between the deposited Ni-Co-S material and electrolyte that benefits the electrochemical performance of the electrode. The selected area electron diffraction (SAED) pattern in Fig. 4(c) indicates a polycrystalline nature of the Ni-Co-S nanosheets. The diffraction rings can be readily indexed to the (222), (331), (422) planes (JCPDS 24-0334) and are consistent with the spinel Ni_2CoS phase. In addition, the HRTEM image in Fig. 4(d) reveals the Ni-Co-S nanosheets are composed of numerous closely packed nanoparticles. A set of lattice fringes with spacing around 0.23 nm can be seen in the HRTEM image, strongly corresponding to the distance of the (400) planes of Ni-Co-S phase (JCPDS 24-0334).

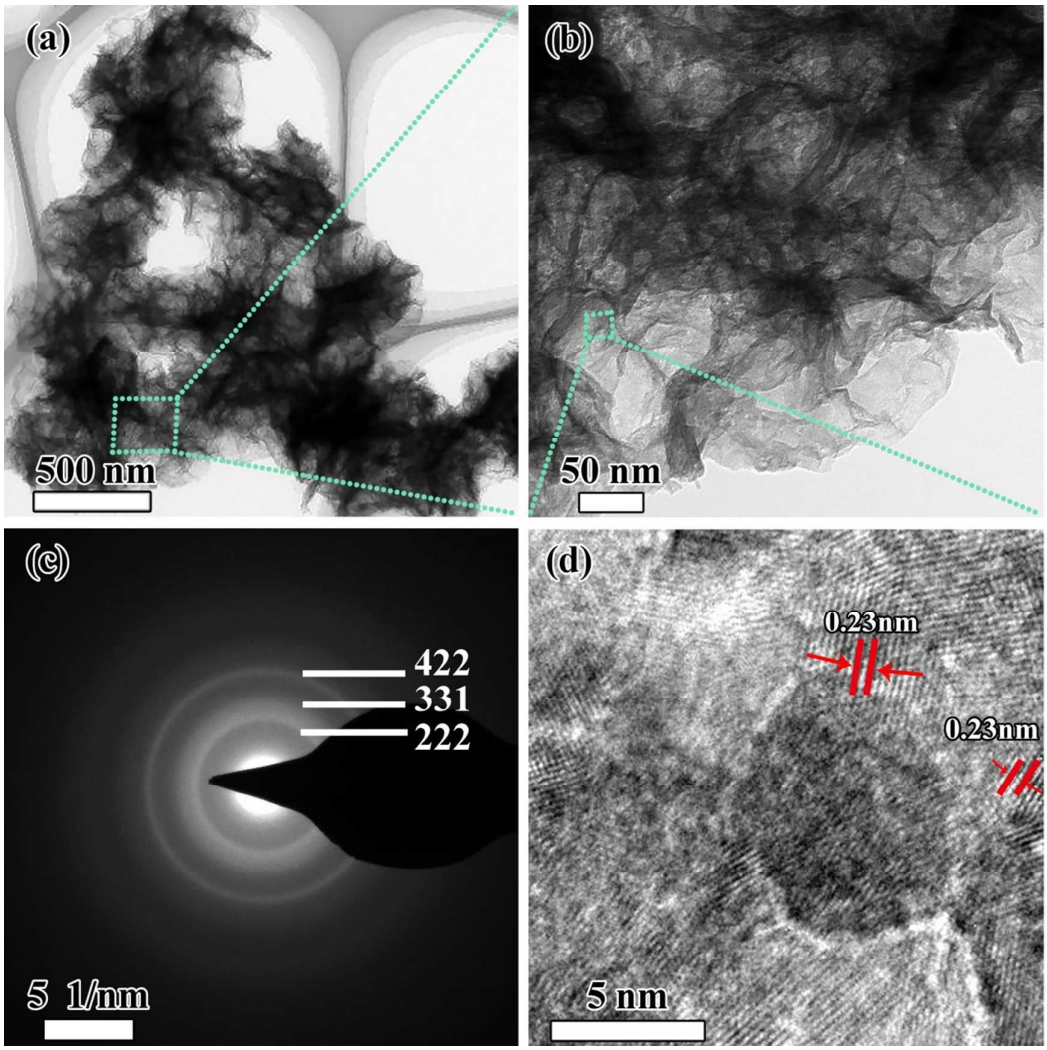

Fig. 4. TEM images of Ni-Co-S/RGO composite: (a) Ni-Co-S/RGO composite, (b) magnified image, (c) SAED patterns, (d) HRTEM image.

XPS measurements were carried out to get additional information about the chemical bond state and the composition of Ni-Co-S/RGO/NF. The results of C 1s, Ni 2p, Co 2p, and S 2p spectra are displayed in Fig. 5 by using the Gaussian fitting method. For the C 1s spectrum in Fig. 5(a), the peaks located at the 284.4, 285.7, 287.8 and 288.9 eV are attributed to the C-C, C-O, C=O and O-C=O bonds, respectively.[26] Fig. 5(a) demonstrates that the RGO nanosheets maintain some oxygenated functional groups after heat reduction. In Fig. 5(b), the Ni 2p spectrum can be fitted to two spin-orbit doublets which are characteristic of Ni^{2+} and Ni^{3+} and two shake-up satellites (denoted as "Sat."). One pair binding energies at 854.6 and 872.4 eV correspond to Ni $2p_{3/2}$ and Ni $2p_{1/2}$, respectively. Another pair is around 856.1 and 875.1 eV. Two pairs of doublets indicate that Ni^{2+} and Ni^{3+} valences exist in the sample.[28, 29] For the Co 2p spectrum in Fig. 5(c), the peaks at 775.4 and 795.8 eV correspond to Co^{2+} and the peaks at 780.7 and 798.6 eV correspond to Co^{3+}. In Fig. 5(d), the S 2p spectrum is divided into two parts.[30] The peak at 164.2 eV is typical for metal-sulfur bonds in ternary metal sulfides and the peak at 168.7 eV is corresponding to the sulfur ion with higher oxide state of $S_4O_6^{2-}$ at the surface.[31-33]

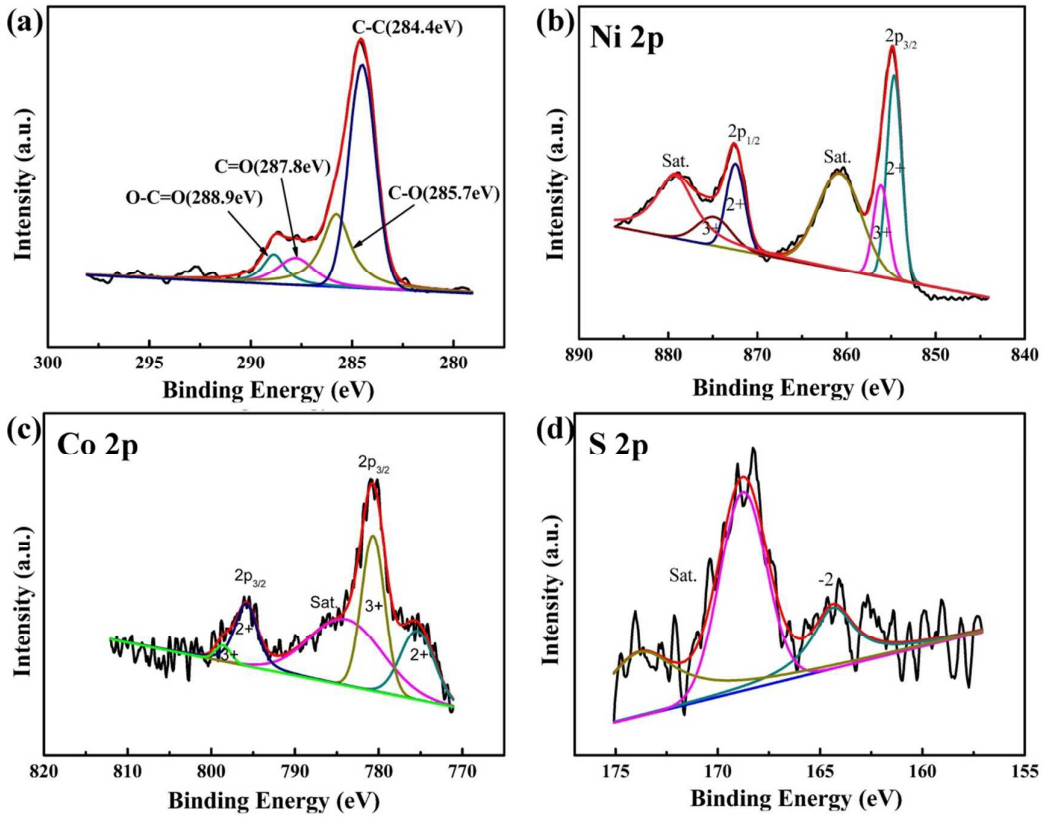

Fig. 5. XPS spectra of Ni-Co-S/RGO: (a) C 1s, (b) Ni 2p, (c) Co 2p and (d) S 2p.

Electrochemical performance

Properties of Ni-Co-S/RGO/NF, Ni-Co-S/GO/NF and Ni-Co-S/NF composites were further investigated by CV and GCD measurements. Fig. 6(a) presents CV curves at a scan rate of 40 mV s-1 within a potential range of -0.2 to 0.8 V. The redox peaks shift to a higher potential for the composites with different substrates (NF, GO/NF and RGO/NF). The reason is as followed: it is well known that according to the basic principle of CV measurement for irreversible and quasi-reversible systems, the diffusion process of ions is a key issue for the peak voltage of the electrode, the lower the diffusion ability is, the higher the peak voltage is. For the electrodes with different substrates (NF, GO/NF and RGO/NF), the microstructures of the electrodes are different. Compared with Ni-Co-S/NF, more porous and hierarchical structures exist for the Ni-Co-S/GO/NF and Ni-Co-S/RGO/NF electrodes as shown in Fig. 2(b), 2(d) and 2(f). So the diffusion process is easier for Ni-Co-S/NF compared with Ni-Co-S/GO/NF and Ni-Co-S/RGO/NF electrodes. In addition, it can be found that the pores in the Ni-Co-S/RGO/NF electrode are smaller than that in Ni-Co-S/GO/NF electrode. So the ion diffusion ability in the Ni-Co-S/GO/NF electrode is higher than that in Ni-Co-S/RGO/NF electrode. As a result, the peak voltages shift to higher potential with the sequence of Ni-Co-S/NF, Ni-Co-S/GO/NF and Ni-Co-S/RGO/NF. The CV curves have a pair of redox peaks that are in agreement with the typical behavior of cobalt sulfides and nickel sulfides previously reported.[34-36] The pair of redox peaks of Ni-Co-S/RGO/NF, Ni-Co-S/GO/NF and Ni-Co-S/NF occur at about 0.67 and -0.05 V, 0.62 and -0.004 V, 0.59 and 0.04 V, respectively. The corresponding voltage potential is attributed to the reversible redox reactions of Ni^{+2}/ Ni^{+3}, Co^{+2}/ Co^{+3} and Co^{+3}/ Co^{+4}. The redox mechanism with the association of alkaline solutions can be summarized as the followed formulas: [24, 37, 38]

$$CoNi_2S_4 + 2OH^- \leftrightarrow CoS_{2x}OH + Ni_2S_{4-2x}OH + 2e^-$$

$$CoS_{2x}OH + OH^- \leftrightarrow CoS_{2x}O + H_2O + e^-$$

The electrochemical performance was further studied by GCD characterization. The GCD curves are illustrated in Fig. 6(b) and are measured in the potential range of 0 to 0.5 V while at a current density of 10 A g^{-1}. The specific capacitances of the active electrode material were calculated from the GCD curves by the following equation:

$$C = I \times \Delta t / (m \times \Delta V) \quad (1)$$

where C (F g^{-1}) is the mass specific capacitance of active electrode material, I (A) is the discharge current, m (g) is the mass of active electrode material, Δt (s) and ΔV (V) are the total discharge time and potential range during one full discharge process, respectively. The specific capacitances of Ni-Co-S/RGO/NF, Ni-Co-S/GO/NF, Ni-Co-S/NF at the current density of 10 A g^{-1} were 2643, 2085 and 1351 F g^{-1}, respectively. These specific

capacitances are consistent with the SEM images in which the ultrathin, flowerlike, interconnected and hierarchical porous ternary Ni-Co-S nanosheets facilitate an increase in the capacitance.

CV curves of the Ni-Co-S/RGO/NF at different scan rates are displayed in Fig. 6(c). A pair of redox peaks can be found for each CV curve. The anodic peaks shift to a higher potential while cathodic peaks shift to a lower potential, indicative of the trend for an irreversible process with an increase of scan rate from 10 to 50 mV s^{-1}. The CV curves are consistent with the features of typical cobalt sulfide and nickel sulfide.[14, 39, 40] The GCD curves of Ni-Co-S/RGO/NF electrode with current densities ranging from 10 A g^{-1} to 50 A g^{-1} are shown in Fig. 6(d). In Fig. 6(e), the specific capacitances of Ni-Co-S/RGO/NF are calculated by equation (1) from the corresponding GCD curves and were found to be 2643, 2276, 2086, 1932, and 1796 F g^{-1} at the current densities of 10, 20, 30, 40 and 50 A g^{-1}, respectively. It can also be found that the specific capacitance of Ni-Co-S/RGO/NF is the largest amongst the three electrode materials at each current density. For example, the specific capacitance of Ni-Co-S/RGO/NF (2643 F g^{-1}) is the highest among the three electrodes at a current density of 10 A g^{-1}; the specific capacitance of Ni-Co-S/GO/NF (2083 F g^{-1}) and Ni-Co-S/NF (833 F g^{-1}) demonstrate a 21.2 % and a 68.5 % reduction relative to Ni-Co-S/RGO/NF, respectively. The rate capabilities of Ni-Co-S/RGO/NF, Ni-Co-S/GO/NF and Ni-Co-S/NF at a current density range of 10 A g^{-1} to 50 A g^{-1} are 68.0, 40.0 and 29.8 %, respectively. Thus, the Ni-Co-S/RGO/NF electrode possesses both enhanced specific capacitance and ideal rate capability.

It is worth noting that the specific capacitance of Ni-Co-S/RGO/NF is superior relative to their materials based on the Ni-Co-S material on carbon cloth via electrochemical deposition (1418 F g^{-1} at a current density of 5 A g^{-1}),[24] the $CoNi_2S_4$ material on graphene via solvothermal method (1046.4 F g^{-1} at a current density of 20 A g^{-1})[33] and $NiCo_2S_4/MnO_2$ via hydrothermal method (1337.8 F g^{-1} at a current density of 2 A g^{-1})[22] Herein, the 3D RGO is capable of providing a suitable conductive substrate for electron flow and possesses a large contact area for the deposition of Ni-Co-S nanosheets. The unique structure of interconnected pores allows the hierarchical Ni-Co-S/RGO/NF electrode to provide a large contact area that is accessible by electrolyte ions that enhances the electrochemical performance of the electrode.

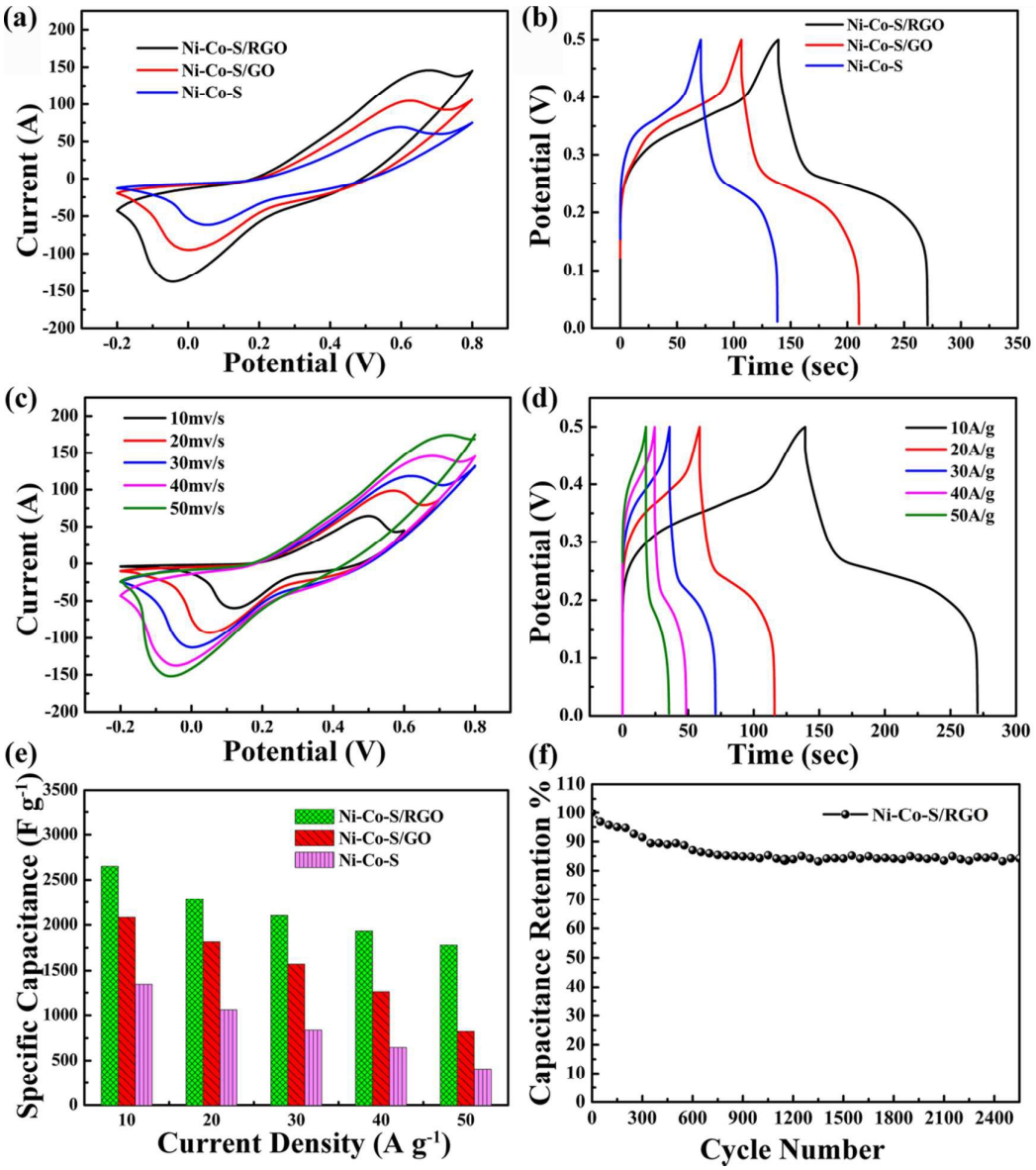

Fig. 6. Electrochemical performances of Ni-Co-S/RGO, Ni-Co-S/GO and Ni-Co-S nanosheet arrays on Ni foam as a supercapacitor electrode by the three-electrode configuration with a 1 M KOH solution as the electrolyte. (a) CV curves at a scan rate of 40 mV s^{-1} and (b) GCD curves of Ni-Co-S/RGO, Ni-Co-S/GO, and Ni-Co-S electrodes at a current density of 10 A g^{-1}; (c) CV curves and (d) GCD curves of Ni-Co-S/RGO electrode at different scan rates; (e) the specific capacitances of the Ni-Co-S/RGO, Ni-Co-S/GO, and Ni-Co-S electrodes at different current densities; (f) the cycle stability of Ni-Co-S/RGO at a current density of 50 A g^{-1}.

The cycle stability is an essential factor for faradaic pseudocapacitor properties due to their typical degradation. As shown in Fig. 6(f), the electrochemical stability of Ni-Co-S/RGO/NF electrode was examined at the current density 50 A g^{-1} in 1 M KOH solution by GCD. After 2500 cycles, the retention of capacity is 84.22 % and the loss of capacity is only 15.78 % when the capacity decreases from 1701.32 F g^{-1} to 1432.85 F g^{-1}. Thus, the Ni-Co-S/RGO/NF electrode has adequate cycle stability that is an essential element for supercapacitor applications.

Electrochemical impedance spectroscopy was investigated in 1 M KOH solution at the frequency range of 0.1 Hz to 100 kHz. As shown in Fig. 7, the Nyquist plot consists of a semi-circular shape in the high frequency region and becomes more linear in the low frequency region.[22, 41, 42] We can obtain information of three types of resistances from the Nyquist plot. Firstly, the equivalent series resistance (R_s) is obtained by the intercept of the Nyquist plot at high frequency (in the inset of Fig. 7), which models the intrinsic impedance of the sample, the contact impedance of the electrode materials and the ohmic resistance of the electrolyte.[43, 44] The magnitudes of R_s for Ni-Co-S/RGO/NF, Ni-Co-S/GO/NF and Ni-Co-S/NF are 1.49, 1.36 and 1.48 Ω, respectively, as shown in the

inset of Fig. 7. The observed marginal difference and minimal values indicate that the conductivity of the electrode materials is comparable to conventional supercapacitors.[45] Secondly, the semicircle in the high frequency region determines the charge-transfer resistance (R_{ct}), which occurs at the surface of the electrode and electrolyte during an electrochemical reaction.[42] The bigger the semicircle is, the higher the R_{ct} value is.[33] The smallest semicircle of Ni-Co-S/RGO/NF electrode material indicates that the lowest electronic resistance between electrode and electrolyte occurs for this material compared with Ni-Co-S/NF and Ni-Co-S/GO/NF, as shown in the inset of Fig. 7. This result demonstrates that the electron conductivity of Ni-Co-S/RGO/NF electrode is promoted by the 3D structure of the RGO nanosheets.[46] Thirdly, the Warburg resistance (Z_w), the slope of the 45° portion of the curve in the low frequency region, is related to the frequency dependence of ion diffusion between electrolyte and electrode interface.[47, 48] For ideal supercapacitors, the slope in the low frequency should be vertical and parallel to the imaginary part of the axis.[43, 49] The nearly vertical line demonstrates that the fast behavior of ion diffusion is capable of yielding enhanced capacitance.[50, 51] As shown in Fig 7, the vertical line in the low frequency region of Ni-Co-S/RGO/NF is the steepest, which demonstrates adequate capacitive behavior without diffusion limitations. The Nyquist impedance plot demonstrates that the Ni-Co-S/RGO/NF has the lowest impedances among the three electrodes. A suitable conductivity for Ni-Co-S/RGO/NF based on the electrochemical impedance results is imperative for the fast changing and discharging processes of redox reactions; thus, the bulk high performance is achieved.

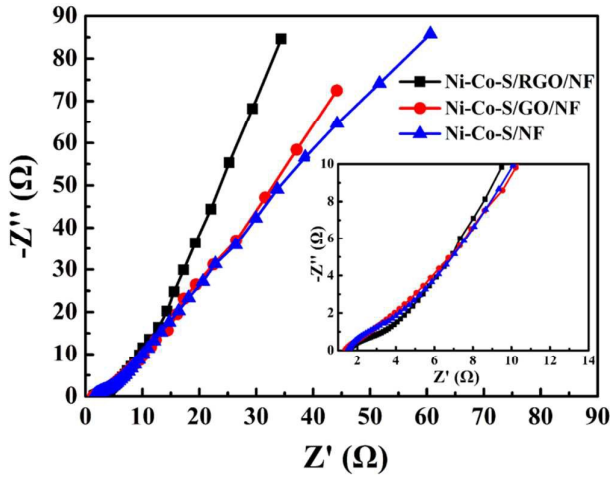

Fig. 7. Nyquist impedance plots of Ni-Co-S/RGO/NF, Ni-Co-S/GO/NF and Ni-Co-S/NF electrode, inset is the magnification of the high-frequency region.

The high performance of the Ni-Co-S/RGO/NF electrode can be attributed to the following factors. One the one hand, 3D RGO can provide both the good conductivity substrate for electron and act as a substrate with a large contact area for the deposition of Ni-Co-S nanosheets. The unique structure of interconnected porous, hierarchical Ni-Co-S/RGO/NF electrode can provide substantial contact surface area reached by electrolyte ions, which can obviously promote the performance of the electrode. On the other hand, good conductivity of Ni-Co-S/RGO/NF, according to the results electrochemical impedances, is beneficial for the fast changing and discharging in the process of redox reaction. As a result, the high electrochemical performance is achieved.

Conclusions

In summary, ultrathin, interconnected porous Ni-Co-S arrays were successfully synthesized by a one-step electrochemical deposition on the 3D GO/NF and 3D RGO/NF substrates. Ni-Co-S/RGO/NF exhibited the highest specific capacitance (2643 F g^{-1}) compared with Ni-Co-S/GO/NF (2083 F g^{-1}) and Ni-Co-S/ NF (1329 F g^{-1}) at the current density of 10 A g^{-1}. The rate capabilities of Ni-Co-S/RGO/NF, Ni-Co-S/GO/NF and Ni-Co-S/NF at current densities from 10 A g^{-1} to 50 A g^{-1} are 68.0 %, 40.0 % and 29.8 %, respectively. Meanwhile, the cycle stability of Ni-Co-S/RGO/NF for 2500 cycles is 84.22 % at the current density of 50 A g^{-1}. The high performance of Ni-Co-S/RGO/NF can be attributed to the following factors: (1) the 3D GO or RGO nanosheets coated on NF provides a large contact area between the deposited Ni-Co-S material and electrolyte, (2) the 3D RGO facilitates ion diffusion in the electrolyte and increases the surface area for redox reactions, and (3) the hierarchical porous structure of the electrode and the synergistic effect of 3D RGO and Ni-Co-S arrays promote an overall high performance in the bulk device. In conclusion, this work demonstrates that Ni-Co-S/RGO/NF is a promising

electrode material for high performance supercapacitor applications.

Acknowledgements

The authors gratefully acknowledge the support from the Harbin Key Technologies R&D Programme (2012DB2CP029).

Notes and references

1 P. G. Bruce, S. A. Freunberger, L. J. Hardwick and J. M. Tarascon, *Nat. Mater.*, 2012, **11**, 19-29.
2 R. D. L. Smith, M. S. Prevot, R. D. Fagan, Z. P. Zhang, P. A. Sedach, M. K. J. Siu, S. Trudel and C. P. Berlinguette, *Science*, 2013, **340**, 60-63.
3 J. Chmiola, C. Largeot, P. L. Taberna, P. Simon and Y. Gogotsi, *Science*, 2010, **328**, 480-483.
4 P. Simon and Y. Gogotsi, *Nat. Mater.*, 2008, **7**, 845-854.
5 G. P. Wang, L. Zhang and J. J. Zhang, *Chem. Soc. Rev.*, 2012, **41**, 797-828.
6 G. A. Snook, P. Kao and A. S. Best, *J. Power Sources*, 2011, **196**, 1-12.
7 C. Guan, X. L. Li, Z. L. Wang, X. H. Cao, C. Soci, H. Zhang and H. J. Fan, *Adv. Mater.*, 2012, **24**, 4186-4190.
8 H. Yang, S. Kannappan, A. S. Pandian, J.-H. Jang, Y. S. Lee and W. Lu, *J. Power Sources*, 2015, **284**, 146-153.
9 X. Wang and G. Shi, *Energy Environ. Sci.*, 2015, **8**, 790-823.
10 L. L. Zhang, X. Zhao, M. D. Stoller, Y. W. Zhu, H. X. Ji, S. Murali, Y. P. Wu, S. Perales, B. Clevenger and R. S. Ruoff, *Nano Lett.*, 2012, **12**, 1806-1812.
11 T. L. Gu and B. Q. Wei, *Nanoscale*, 2015, **7**, 11626-11632.
12 K. Liang, T. L. Gu, Z. Y. Cao, X. Z. Tang, W. C. Hu and B. Q. Wei, *Nano Energy*, 2014, **9**, 245-251.
13 N. Terasawa and K. Asaka, *Langmuir*, 2014, **30**, 14343-14351.
14 Y. C. Mao, W. Li, P. Liu, J. Chen and E. J. Liang, *Mater. Lett.*, 2014, **134**, 276-280.
15 J. Y. Ji, L. L. Zhang, H. X. Ji, Y. Li, X. Zhao, X. Bai, X. B. Fan, F. B. Zhang and R. S. Ruoff, *Acs Nano*, 2013, **7**, 6237-6243.
16 H. Hu, B. Y. Guan, B. Y. Xia and X. W. Lou, *J. Am. Chem. Soc.*, 2015, **137**, 5590-5595.
17 Y. H. Li, L. J. Cao, L. Qiao, M. Zhou, Y. Yang, P. Xiao and Y. H. Zhang, *J. Mater. Chem. A*, 2014, **2**, 6540-6548.
18 H. C. Chen, J. J. Jiang, L. Zhang, D. D. Xia, Y. D. Zhao, D. Q. Guo, T. Qi and H. Z. Wan, *J. Power Sources*, 2014, **254**, 249-257.
19 Q. Liu, J. T. Jin and J. Y. Zhang, *Acs Appl. Mater. Interfaces*, 2013, **5**, 5002-5008.
20 J. W. Xiao, X. W. Zeng, W. Chen, F. Xiao and S. Wang, *Chem. Commun.*, 2013, **49**, 11734-11736.
21 L. Yu, L. Zhang, H. B. Wu and X. W. Lou, *Angew. Chem. Int. Edit.*, 2014, **53**, 3711-3714.
22 J. Yang, M. Ma, C. Sun, Y. Zhang, W. Huang and X. Dong, *J. Mater. Chem. A*, 2015, **3**, 1258-1264.
23 G. Q. Zhang and X. W. Lou, *Adv. Mater.*, 2013, **25**, 976-979.
24 W. Chen, C. Xia and H. N. Alshareef, *Acs Nano*, 2014, **8**, 9531-9541.
25 V. H. Nguyen, C. Lamiel and J. J. Shim, *Electrochim. Acta*, 2015, **161**, 351-357.
26 J. Yang, C. Yu, X. Fan, C. Zhao and J. Qiu, *Adv. Funct. Mater.*, 2015, **25**, 2109-2116.
27 S. Park and R. S. Ruoff, *Nat. Nanotechnol.*, 2009, **4**, 217-224.
28 W. Hu, R. Q. Chen, W. Xie, L. L. Zou, N. Qin and D. H. Bao, *ACS Appl. Mater. Interfaces*, 2014, **6**, 19318-19326.
29 G. X. Gao, H. B. Wu, S. J. Ding, L. M. Liu and X. W. Lou, *Small*, 2015, **11**, 804-808.
30 H. Z. Wan, J. Liu, Y. J. Ruan, L. Lv, L. Peng, X. Ji, L. Miao and J. J. Jiang, *Acs Appl. Mater. Interfaces*, 2015, **7**, 15840-15847.
31 J. H. Tang, J. F. Shen, N. Li and M. X. Ye, *Ceram. Int.*, 2015, **41**, 6203-6211.
32 J. Xu, L. Li, P. Gao, L. Yu, Y. Chen, P. Yang, S. Gai and P. Yang, *Electrochim. Acta*, 2015, **166**, 206-214.
33 W. M. Du, Z. Y. Wang, Z. Q. Zhu, S. Hu, X. Y. Zhu, Y. F. Shi, H. Pang and X. F. Qian, *J. Mater. Chem. A*, 2014, **2**, 9613-9619.
34 Z. M. Zhang, Q. Wang, C. J. Zhao, S. D. Min and X. Z. Qian, *Acs Appl. Mater. Interfaces*, 2015, **7**, 4861-4868.
35 J. Xu, Q. F. Wang, X. W. Wang, Q. Y. Xiang, B. Hang, D. Chen and G. Z. Shen, *Acs Nano*, 2013, **7**, 5453-5462.
36 X. Y. Yan, X. L. Tong, L. Ma, Y. M. Tian, Y. S. Cai, C. W. Gong, M. G. Zhang and L. P. Liang, *Mater. Lett.*, 2014, **124**, 133-136.
37 X. Y. Liu, Y. Q. Zhang, X. H. Xia, S. J. Shi, Y. Lu, X. L. Wang, C. D. Gu and J. P. Tu, *J. Power Sources*, 2013, **239**, 157-163.
38 Y. Zhang, M. Ma, J. Yang, C. Sun, H. Su, W. Huang and X. Dong, *Nanoscale*, 2014, **6**, 9824-9830.
39 W. T. Wei, L. W. Mi, Y. Gao, Z. Zheng, W. H. Chen and X. X. Guan, *Chem. Mater.*, 2014, **26**, 3418-3426.
40 Y. J. Li, K. Ye, K. Cheng, J. L. Yin, D. X. Cao and G. L. Wang, *J. Power Sources*, 2015, **274**, 943-950.
41 G. Li and C. Xu, *Carbon*, 2015, **90**, 44-52.
42 Y. Z. Xu, J. C. Wei, L. C. Tan, J. Yu and Y. W. Chen, *J. Mater. Chem. A*, 2015, **3**, 7121-7131.
43 B. Wei, L. D. Wang, Q. H. Miao, Y. N. Yuan, P. Dong, R. Vajtai and W. D. Fei, *Carbon*, 2015, **85**, 249-260.
44 M. D. Stoller, S. J. Park, Y. W. Zhu, J. H. An and R. S. Ruoff, *Nano Lett.*, 2008, **8**, 3498-3502.
45 Z. Y. Zhang, F. Xiao, L. H. Qian, J. W. Xiao, S. Wang and Y. Q. Liu, *Adv. Energy Mater.*, 2014, **4,** 1400064.
46 J. Yan, Q. Wang, C. P. Lin, T. Wei and Z. J. Fan, *Adv. Energy Mater.*, 2014, **4,** 1400500.
47 J. Tao, N. Liu, L. Li, J. Su and Y. Gao, *Nanoscale*, 2014, **6**, 2922-2928.
48 J. Xiao, L. Wan, S. Yang, F. Xiao and S. Wang, *Nano Lett.*, 2014, **14**, 831-838.
49 R. B. Rakhi, W. Chen, D. Cha and H. N. Alshareef, *Adv. Energy Mater.*, 2012, **2**, 381-389.

50 M. Kim, Y. Yoo and J. Kim, *J. Power Sources*, 2014, **265**, 214-222.
51 T. Bordjiba and D. Belanger, *J. Electrochem. Soc.*, 2009, **156**, A378-A384.